

Dislocation Arrangements and Cyclic Microplasticity Surrounding Stress Concentration in a Ni-Based Single-Crystal Superalloy

Alessandro Piglione, Tom Bellamy, Jian Yu, Jinqian Zhao, Chengbo Xiao, Fionn P. E. Dunne, and Minh-Son Pham*


Local cyclic plasticity near stress concentrations governs the fatigue crack initiation in cyclicly loaded Ni-based single-crystal superalloys, but has not been well studied and understood. The first of its kind transmission electron microscopy (TEM)-based site-specific study of plasticity in the crack initiation region in a notched single-crystal superalloy subjected to fatigue testing at 800 °C, coupling it with microstructure-based crystal plasticity modeling, is presented. Detailed TEM examinations show that local plasticity near the notch significantly differs from bulk plasticity, featuring high dislocation densities and distinctive arrangements of dislocation pairs within γ' precipitates. It further shows that the increased local stresses alone are responsible for the increase in dislocation density and extensive γ' shearing, but not solely for the distinctive arrangement of dislocation pairs seen in the notch vicinity, thus highlighting the considerable role played by the local variations in loading rates and stress state surrounding the notch. The results of this work provide new fundamental insights into the deformation micromechanisms leading to fatigue crack initiation in single-crystal superalloys.

1. Introduction

Ni-based superalloys offer outstanding mechanical properties at elevated temperatures coupled with good resistance to aggressive environments and are therefore widely employed for the fabrication of first-stage turbine blades in both jet engines for aircraft

A. Piglione, T. Bellamy, F. P. E. Dunne, M.-S. Pham
Department of Materials
Imperial College London
Exhibition Road, London SW7 2AZ, UK
E-mail: son.pham@imperial.ac.uk

J. Yu, J. Zhao, C. Xiao
Science and Technology on Advanced High Temperature Structural
Materials Laboratory
Beijing Institute of Aeronautical Materials
Beijing 100095, China

 The ORCID identification number(s) for the author(s) of this article can be found under <https://doi.org/10.1002/adem.202300602>.

© 2023 Imperial College London. Advanced Engineering Materials published by Wiley-VCH GmbH. This is an open access article under the terms of the Creative Commons Attribution License, which permits use, distribution and reproduction in any medium, provided the original work is properly cited.

DOI: 10.1002/adem.202300602

propulsion and industrial gas turbines for power generation. Such blades are subjected to complex loading conditions in operation including cyclic loads at elevated temperatures.^[1–3] As a consequence, blade failure may occur following the nucleation and propagation of fatigue cracks from stress concentration sites such as interdendritic pores,^[3–6] which form during casting, or cooling holes,^[7–10] which are used to control the temperature of the blades in operation. Since crack initiation is associated with a localized accumulation of plastic micro-strains, the fatigue lives are governed by local cyclic plasticity developing in low-angle grain boundaries and in proximity of stress concentrations such as cast pores or cooling ducts rather than by bulk plasticity.^[3,5,11] In addition, with an increasing use of additive manufacturing for Ni superalloys^[12–14] in which pores or surface notches are found to be the main

sites for fatigue crack initiation in additively manufactured alloys,^[15–17] in-depth knowledge of microplasticity surrounding stress raisers (such as surface notches and pores) is ever needed to understand the crack initiation to ensure the performance and reliability of alloys. However, cyclic plasticity developing in single-crystal superalloys subjected to fatigue loading is most often studied in the bulk of the material (e.g.,^[18–25]). The limitation of this approach lies in the fact that stress concentrations not only increase the local stress levels, but also locally modify the stress state^[8–10]; in addition, the increased stress levels result in higher loading rates compared to the nominal ones.^[26] Such local modifications translate into distinctive differences between bulk and local plasticity near stress concentrations, as the development of plasticity in single-crystal superalloys, which feature a peculiar double-phase microstructure consisting of a high volume fraction ($\approx 70\%$) of coherent cuboidal γ' precipitates orderly distributed in thin γ matrix channels, is a complex function of both stress state and strain rate.^[18,21] There is, therefore, a strong need to investigate the development of local cyclic plasticity near stress concentrations to gain a better understanding of crack initiation in single-crystal superalloys.

While the dislocation interaction and subsequent arrangements at the interface between γ' precipitates and the matrix to accommodate the lattice mismatch have been

well studied,^[27–30] very few studies have been dedicated to the investigation of dislocation arrangements in regions surrounding stress concentrations to better understand the fatigue crack initiation. One important contribution in this regard was recently provided by Cervellon et al.,^[31] who studied local deformation near the pores that induced fatigue crack initiation in two single-crystal superalloys tested at 1000 °C with 20 kHz. They showed that, in contrast with the mostly undeformed bulk regions in each test piece, intense deformation and extensive γ' shearing occurred near pores, leading to recrystallization and precipitation of new phases, and finally a model was proposed for fatigue crack initiation.^[31] This study highlighted the necessity of investigating local microplasticity at stress raisers in superalloys subjected to cyclic loading. However, experimental studies of local plasticity were limited to electron channeling contrast imaging, and detailed dislocation analyses at the initiation sites were not performed. More generally, to the best of the author's knowledge, direct observations of local cyclic plasticity near stress concentrations in fatigued single-crystal superalloys by means of transmission electron microscopy (TEM) have not been reported yet. TEM studies enable more detailed examinations of local plasticity, including the identification of the γ' shearing mechanisms, of the active slip systems, and of the characters of the dislocations.

In our recent investigation,^[32] focused ion beam (FIB) lift-outs were performed to obtain thin foils for TEM from regions surrounding a notch in a specimen fatigued at 800 °C with macroscopic elastic cyclic loads. It was shown that local cyclic plasticity near the notch differed significantly from that in the bulk of the test piece, with high dislocation densities and extensive γ' shearing in contrast to isolated plasticity developing only in the γ channels.^[32] Such observations highlighted the importance of investigating local deformation near stress raisers, as well as the need for further work aimed at deepening the understanding of not only the degree of slip and γ' shearing, but also the arrangement of dislocations in γ' shearing of locations near such notches in relation to the stress field around the notch itself; this is the purpose of the present work.

To complement the study of the dislocation substructure evolution in the region near the notch, a crystal plasticity finite-element model (CPFEM) was used to estimate the local stress state and plasticity surrounding the notch by accounting for its measured size and shape and for the measured crystallographic orientation of the test piece relative to the loading direction (LD) and to the notch itself. In addition, further detailed microscopic studies were carried out to investigate in greater detail the dislocations within the γ' precipitates and in particular to determine the shearing mechanisms and the active slip systems in the region near the notch. Such investigations were performed postmortem and could therefore not provide insights into local plasticity in the early loading cycles. Hence, a representative volume element (RVE) model of the γ/γ' microstructure, accounting in particular for the morphology and relative strengths of the two phases, was then used to predict the development of local microplasticity in the first few loading cycles. The results presented in this work provide new fundamental insight into the development of local

plasticity near stress concentrations in fatigued single-crystal superalloys.

2. Experimental Section

2.1. Materials

The alloy selected for this work was the DD6 Ni-based single-crystal superalloy; its nominal composition is shown in Table 1.^[33] The castings were cylindrical bars measuring 15 mm in diameter and 150 mm in length. Such bars were subjected to the following heat treatment in vacuum: 1290 °C/1 h + 1300 °C/2 h + 1315 °C/4 h + air cooling (AC), 1120 °C/4 h + AC, 870 °C/32 h + AC. The microstructure of the alloy consisted of an ordered distribution of coherent cuboidal γ' precipitates in the γ matrix. In particular, the alloy was characterized by a γ' volume fraction of $\approx 70\%$, and the cube edge length of the precipitates was ≈ 450 nm.

2.2. Experimental Procedure

The test in this work was carried out on a single-crystal cylindrical test piece with a gauge diameter of 5.5 mm and a gauge length of 15 mm. The longitudinal (loading) axis of the test piece was within 10° of the [001] crystal orientation. Its gauge section had a roughness average R_a of 0.4 μm . To facilitate the investigation of local plasticity, a notch was created on the specimen before the test using a multiaxis computer numerical control electrical discharge machine (EDM). Such a notch was cylindrical in shape, with nominal depth and diameter of 300 μm to simulate cooling holes. The fully reversed ($R = -1$) fatigue test was carried out in air at 800 °C, with the load applied uniaxially along the longitudinal direction of the test piece. The test was performed in strain control imposing a triangular waveform with a strain amplitude of 0.6% at a strain rate of $5 \times 10^{-3} \text{ s}^{-1}$ using an MTS Landmark servohydraulic test system equipped with a 12 mm-high temperature extensometer. The imposed strain amplitude was lower than the yield strain of the alloy at 800 °C (about 60% of the macroyield strain, Figure A.1). This choice of strain amplitude resulted in considerable microplasticity surrounding the notch to study the effect of the notch while the nominal deformation was still in the elastic loading regime. Load and displacement data was recorded for selected cycles during the test.

2.3. Characterization

Postmortem fractographic analyses were carried out using a Zeiss Auriga and a Zeiss Sigma 300 scanning electron microscopes (SEMs) operating at 20 kV. To study microstructural deformation in the bulk of the test piece, thin foils for transmission electron microscopy (TEM) were sliced from the gauge

Table 1. Nominal composition of the DD6 single-crystal superalloy.^[23]

Element	Ni	Co	Cr	Mo	W	Al	Ta	Re	Nb	Hf
[%wt]	Bal.	9.0	4.3	2.0	8.0	5.6	7.5	2.0	0.5	0.1

section of the notched test piece, normal to its longitudinal direction; as a consequence, these foils had their normal parallel to the LD and therefore very close to [001]. These foils were then ground with fine SiC paper to achieve a thickness of about 100 μm and finally prepared by twin-jet electropolishing in a solution of 10% perchloric acid in methanol applying 20 kV at -5°C with a Struers TenuPol-5. Three of such foils were investigated by TEM to ensure the repeatability of the observations.

To investigate microstructural deformation in the initiation region of the notched specimen, thin foils for TEM were prepared performing FIB lift-outs from using FEI Helios. It was important to relate the observed dislocation arrangements with their location with respect to the notch due to the spatial variation of the multiaxial stress state around the notch itself; to this end, the SEM micrographs in **Figure 1** provide a “map” of the lift-out locations in this study. In particular, Figure 1a shows the fracture surface of the test piece, while Figure 1b shows the regions close to the notch in greater detail. Furthermore, the white dashed line in Figure 1b indicates the line along which the sample was sectioned. An SEM micrograph of the resulting cross section, imaged after mechanical grinding and polishing, is shown in Figure 1c. A number of trenches are visible in both Figure 1b,c, indicating the locations at which FIB lift-outs were performed; the locations of interest for the purpose of this study are marked by red circles and labeled with a number. It is noted that EDM affected a thin layer of material during notch fabrication ($\approx 20\ \mu\text{m}$, as seen in Figure 1c); the lift-outs in this work were therefore carried out at suitable distances from the notch to avoid investigating microstructural deformation in such affected regions.

TEM and scanning TEM (STEM) investigations were carried out using a Jeol JEM-2100F microscope operating at 200 kV. All TEM micrographs in this work, with the exception of those used for the determination of dislocation line vectors, were bright-field (BF) images obtained in two-beam conditions, that is, the images were obtained by exciting a single \mathbf{g} reflection. Each TEM micrograph was complemented by an image of the diffraction pattern of the respective zone axis, together with an arrow indicating the \mathbf{g} reflection used to achieve the two-beam condition. Both the beam direction \mathbf{B} and the reflection \mathbf{g} are indicated in the image captions. The dislocation density was measured in selected micrographs using the line intercept method^[34,35]: a grid of perpendicular test lines was superimposed on each micrograph, and the number of intersections of each test line with dislocation lines was counted. The dislocation density was then calculated as

$$\rho = \frac{1}{t} \frac{\sum_1^N \mathbf{n}_i / L_i}{N} \quad (1)$$

where \mathbf{n}_i is the number of dislocation intersections of the i^{th} grid line, L_i is the length of the i^{th} grid line, N is the number of grid lines, and t is the thickness of the foil from which the image was obtained. The foil thickness was measured from SEM micrographs obtained with the FEI Helios used for the lift-outs. The Burgers vector \mathbf{b} of selected dislocations was determined using the invisibility criterion, which states that a dislocation is invisible in a two-beam condition image formed using a specific \mathbf{g} reflection if \mathbf{g} is normal to \mathbf{b} , or $\mathbf{g} \cdot \mathbf{b} = 0$. Hence, if two such reflections are found, \mathbf{b} can be determined as it is normal to both \mathbf{g} reflections used.^[36] The line direction \mathbf{u} of the dislocations was determined by finding the angle θ between the normal to the projected dislocation line and a \mathbf{g} reflection in three micrographs taken with three different beam directions. Each normal was then plotted in a stereographic projection by measuring the angle θ from the selected \mathbf{g} reflection along the great circle associated with respective beam direction. The line direction \mathbf{u} of the dislocation could then be determined as the pole of the great circle defined by the three normals to the projected dislocation line in the stereographic projection.^[26]

2.4. Crystal Plasticity Finite Element Model (CPFEM)

To estimate the stress state at the locations investigated by TEM and predict the consequent microstructural deformation near the notch, two models were created. First, a finite-element model of the geometry of the notched sample was constructed and subjected to the same fatigue loading undergone by the experimental test sample. This first model represented the γ/γ' microstructure as a homogenized face-centered-cubic (fcc) single crystal with appropriate octahedral slip strength and was used to extract the displacement boundary conditions for a second microscale model, which was aimed at replicating the alloy's detailed γ/γ' microstructure and deformation using RVE. In particular, principal strains from the first model were extracted in the regions where the FIB lift-out was carried out and then used as displacement boundary conditions for the RVE γ/γ' model in order to replicate the conditions at the locations investigated by TEM. Hence differing, tailored RVE models were developed for each of the locations of interest in the experimental sample.

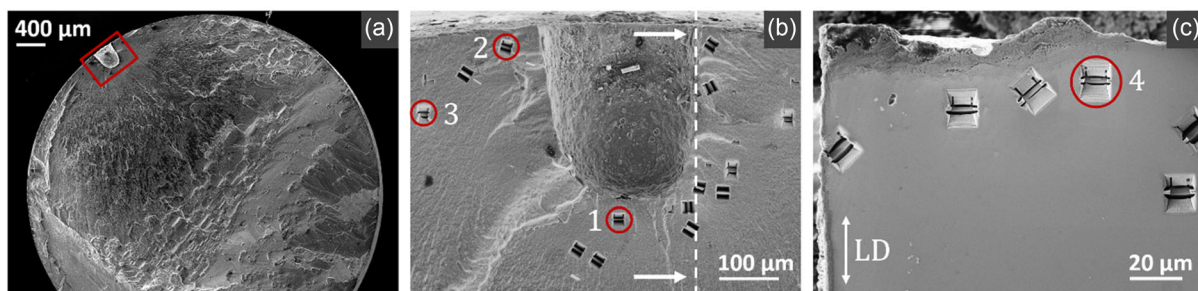


Figure 1. a) SEM micrograph of the fracture surface of the notched test piece; b) magnified view of the regions close to the notch, indicated by the red rectangle in (a); c) SEM micrograph of the cross section of the notch, obtained by sectioning the sample along the white dashed line shown in (b). LD indicates the loading direction. The red circles indicate the FIB lift-out locations that are of interest in this study.

The crystal plasticity slip rule was implemented into ABAQUS. The model considered both elastic and plastic parts of a deformation gradient, \mathbf{F} , written as \mathbf{F}^e and \mathbf{F}^p , respectively, where

$$\mathbf{F} = \mathbf{F}^e \mathbf{F}^p \quad (2)$$

The plastic velocity gradient \mathbf{L}^p is given by

$$\mathbf{L}^p = \dot{\mathbf{F}}^p \mathbf{F}^{p-1} = \sum \dot{\gamma}^\alpha (\mathbf{s}^\alpha \otimes \mathbf{n}^\alpha) \quad (3)$$

where α denotes the differing slip systems, $\dot{\gamma}$ is the slip rate, and \mathbf{s} and \mathbf{n} are the slip direction and slip plane normal, respectively. The slip rate^[37] was prescribed on the basis of thermal activation and escape of pinned dislocations at the slip system level.

$$\dot{\gamma} = \rho_m v_0 b^2 \exp\left(-\frac{\Delta \mathbf{F}}{kT}\right) \sinh\left(\frac{(\tau - \tau_c) \Delta V}{kT}\right) \quad (4)$$

In this formulation, ρ_m is the mobile dislocation density, v_0 the frequency of dislocation attempting to escape obstacle barriers, \mathbf{b} the Burgers vector, k the Boltzmann constant, T the temperature, $\Delta \mathbf{F}$ the activation energy, and ΔV the corresponding activation volume for these pinned dislocation events. The resolved shear stress on a slip system is given by τ and the critical resolved shear stress (CRSS) for the same slip system is τ_c . Rate sensitivity is controlled by the activation energy and the corresponding activation volume.

The CRSS (i.e., the slip strength) of a given slip system is allowed to harden in general through the evolution of statistically stored (SSD) and geometrically necessary (GND) dislocation density according to

$$\tau_c = \tau_{c0} + Gb\sqrt{\rho_{SSD} + \rho_{GND}} \quad (5)$$

In the present work, the SSD density did not evolve from its initial value since the observed hardening was very low. GND density was calculated from the lattice curvature using the Nye tensor $\mathbf{\Lambda}$ given by

$$\mathbf{\Lambda} = \text{curl}(\mathbf{F}^p) = \sum \rho_{Gs} \mathbf{b} \otimes \mathbf{m} + \rho_{Get} \mathbf{b} \otimes \mathbf{t} + \rho_{Gen} \mathbf{b} \otimes \mathbf{n} \quad (6)$$

The dislocation components are ρ_{Gs} (screw), ρ_{Get} (edge), and ρ_{Gen} (edge). The vectors \mathbf{m} , \mathbf{t} , and \mathbf{n} are an orthogonal set for respective slip systems.

The individual GND density on each of the 12 slip systems is described in the work by Cheng and Ghosh.^[38] The methodology uses the tensor \mathbf{A} to determine the overall GND density ρ_{GND} from

$$\mathbf{A} \rho_{GND} = \mathbf{\Lambda} \quad (7)$$

$$\rho_{GND} = \mathbf{A}^+ \mathbf{\Lambda} \quad (8)$$

$$\rho_{GND} = \sqrt{\rho_{Gs}^2 + \rho_{Get}^2 + \rho_{Gen}^2} \quad (9)$$

The notch shape and dimensions for the test sample model were taken from the SEM micrograph in Figure 1b, and the notch profile revolved to approximate its 3D shape. A fully reversed strain of 0.6% was applied to the loading face. The model and the applied loading are shown in Figure 2a,b. The crystallographic orientation of the model single crystal was specified to be the same as that of the test sample relative to both the LD and the notch. Such orientation was determined with a spot electron backscatter diffraction scan carried out within a Zeiss Sigma 300 SEM operating at 20 kV; the Euler angles that related the measured crystal orientation to the reference coordinate system shown in Figure 2 (where the x-axis is parallel to the notch axis) were $\varphi_1 = 99^\circ$, $\Phi = 29^\circ$, $\varphi_2 = 265^\circ$.

In this model, the material was assumed to consist of a single elastically anisotropic ($C_{11} = 189$ GPa, $C_{12} = 100$ GPa, and $C_{44} = 90$ GPa) homogenized fcc γ phase, featuring the 12 octahedral slip systems listed in Table 2. The slip rule properties are listed in Table 3. The value of τ_{c0} was extracted from a monotonic tensile test carried out at 800 °C with a strain rate of 10^{-3} s^{-1} on a DD6 test piece. The strain rate sensitivity of the material was taken to be negligible; this was reflected in the model by selecting an appropriately large value of ΔV . A good representation of the behavior at 800 °C is achieved, provided that the strain rates do

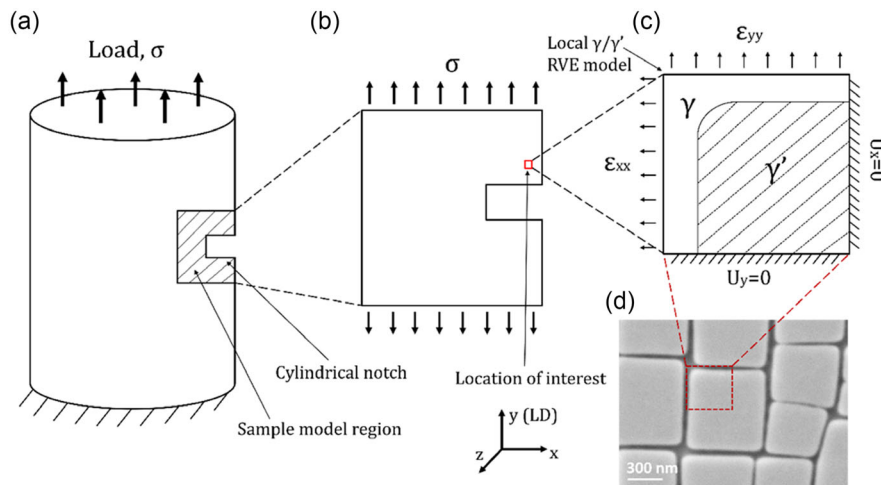


Figure 2. a,b) Schematic diagrams of the notched sample model and of the c) RVE model. d) An SEM micrograph of the γ/γ' microstructure after etching.

Table 2. List of the 12 octahedral slip systems used for the fcc model.

SS no.	Slip plane	Slip direction
1	(11 $\bar{1}$)	[101]
2	(11 $\bar{1}$)	[011]
3	(11 $\bar{1}$)	[1 $\bar{1}$ 0]
4	(1 $\bar{1}$ 1)	[10 $\bar{1}$]
5	(1 $\bar{1}$ 1)	[01 $\bar{1}$]
6	(1 $\bar{1}$ 1)	[110]
7	(111)	[10 $\bar{1}$]
8	(111)	[01 $\bar{1}$]
9	(111)	[1 $\bar{1}$ 0]
10	($\bar{1}$ 11)	[101]
11	($\bar{1}$ 11)	[01 $\bar{1}$]
12	($\bar{1}$ 11)	[110]

not deviate strongly from those utilized for the property extraction, as evidence in the literature^[39] shows limited changes in superalloy yield and tensile strengths over applied strain rate range 10^{-5} – 10^{-3} s⁻¹. The values of the other properties were taken from a study by Chen et al.^[40]

This model was utilized to extract out local strain components at the various regions of interest adjacent to the notch to provide the loading and boundary conditions for the additional local, RVE submodels. The RVE models were developed to incorporate both the γ channels and γ' precipitates explicitly, whose dimensions were based on SEM observations. The γ' precipitates were modeled as cubes with an edge length of 400 nm, while the channel width was set to 60 nm; 1/8th subsection of this geometry was taken to reduce computational time. A schematic diagram of the RVE model and an SEM micrograph of the γ/γ' microstructure of the DD6 superalloy after etching are shown in Figure 2c,d, respectively, in relation to the notched sample model shown in Figure 2a,b. It should be noted that as the RVE is a 3D model, the boundary conditions in the Z direction (not shown in Figure 2c) were equivalent to those in the X and Y directions. The material properties used for the RVE model were identical to those used for the fcc model with the exceptions of the anisotropic elastic moduli and the initial CRSS values for the individual phases; these are listed in **Table 4**. The relative strengths of both phases were determined using available experimental tensile data and sources in the literature. In particular, the anisotropic elastic properties for the matrix phase were taken from a study by Siebörger et al.,^[41] and the elastic properties of the precipitate phase were inferred using this and existing DD6 tensile data by varying the elastic moduli of the precipitate phase to give a linear elastic region with a macroscopic elastic modulus equal to that of the existing tensile data. As TEM studies found

Table 3. Material properties for the homogenized DD6 single-crystal superalloy.

τ_{c0} [MPa]	E [GPa]	G [GPa]	ν	b [μm]	ν_0 [s ⁻¹]	ΔF [J atom ⁻¹]	ρ_{ssdm} [μm^{-2}]	k [JK ⁻¹]	ΔV [μm^3]
430	120	90	0.346	2.54e – 4	1e + 11	3.456e – 20	0.01	1.381e – 23	111b ³

Table 4. Material properties for the two-phase RVE.

τ_{c0} -precipitate [MPa]	$E_{\text{precipitate}}$ [GPa]	$G_{\text{precipitate}}$ [GPa]	$\nu_{\text{precipitate}}$
588	170	90	0.4
τ_{c0} -matrix [MPa]	E_{matrix} [GPa]	G_{matrix} [GPa]	ν_{matrix}
333	90	90	0.4

no evidence of cubic slip, only octahedral slip systems (the same used for the γ matrix listed in Table 2) were considered for γ' precipitates. The CRSS for each independent phase was determined from the DD6 tensile data with reference to similar data for both a binary crystal of Ni₃Al^[42] and of the gamma matrix.^[43,44] The CRSS values at 800 °C were 313 MPa^[32] and 58 MPa^[43,44] for γ' and γ , respectively, but these values were for the basic phases with no additional strength contributions from alloying. To make the phase strengths representative of the yield behavior of DD6, the CRSS values for each phase to obtain macroscopic behavior comparable with the experimental DD6 tensile data were obtained and given in Table 4. A comparison between the experimental stress/strain curve from the tensile test and that generated with the RVE model is shown in Appendix A. The loading conditions for the RVE models were created by applying the local strain state obtained for the four regions of interest, generated as discussed above from the homogenized fcc sample model.

3. Results

3.1. Mechanical Data

The fatigue life of the notched test piece was 2786 cycles, which was much shorter than those (65 045 and 57 786 cycles) of two smooth specimens. Experimental stress and strain data for the first cycle of the notched test piece are shown in **Figure 3a**. The imposed strain was lower than the yield strain of the alloy of study at 800 °C, resulting in a macroscopic elastic response (**Figure 3a**); such a response did not evolve significantly throughout the specimen's fatigue life, as shown in our previous study.^[32] The CPFEM model was used to extract stress/strain curves along the LD. The bulk stress/strain curve for the first cycle obtained using the homogenized fcc sample model is shown in **Figure 3a**; the model reflected the experimentally observed average elastic response of the sample under loading. The γ/γ' RVE model was then used to predict the local stress/strain curves at each of the locations of interest around the notch shown in **Figure 1**; the displacement boundary conditions for each location were extracted from the homogenized fcc sample model. The stress/strain curves for the first loading cycle at each location are shown in **Figure 3b**. The four locations of interest near the notch were predicted to experience significantly larger stresses and strains compared to those in the bulk. The strains

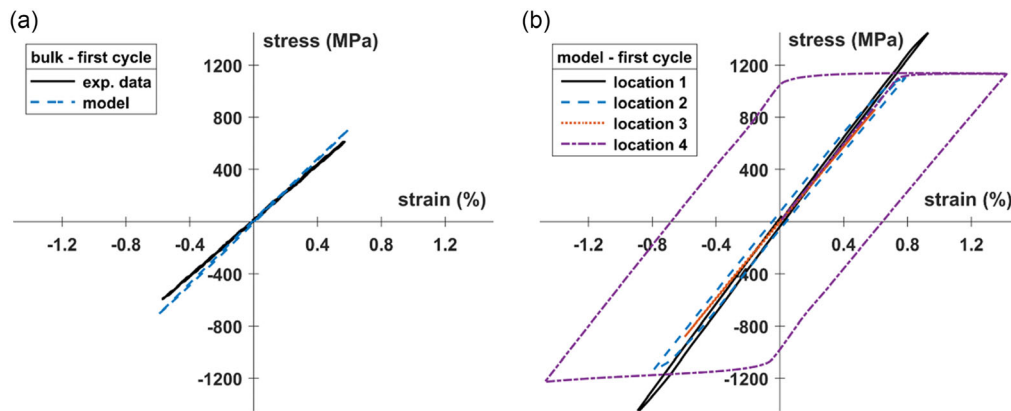


Figure 3. a) Comparison between the experimental stress/strain data for the first fatigue cycle of the notched test piece and the bulk sample model predictions. b) Local stress/strain response in the first fatigue cycle obtained from the RVE model at each of the four locations of interest shown in Figure 1.

in regions 1, 2, and 4 were already in the plastic regime right from the first cycle, while region 3 was found to experience only elastic straining in the first cycle. Among the considered locations, location 4 was subjected to the largest strain, just above 1.4%; this shows that the strains on the side of the notch were larger compared to those at the notch root (see Figure 1 for the lift-out locations). As a consequence, region 4 exhibited the largest amount of plasticity. Region 3, on the other hand, seems far from the notch to be significantly affected by the notch. Region 1 experienced larger strains compared to region 2; however, the latter exhibits more plasticity due to the lower triaxiality in region 2 compared to region 1. Because the regions near the notch were subjected to larger strains compared to the bulk over the same duration of time, the local increase in strain should be accompanied by higher strain rates. In fact, the simulation showed that the location 4 experienced the largest strain rate of $1.2 \times 10^{-2} \text{ s}^{-1}$, more than double the nominal strain rate of $5.0 \times 10^{-3} \text{ s}^{-1}$.

3.2. Bulk Plasticity

Postmortem investigations revealed that plastic deformation in the bulk of the test piece was highly heterogeneous. The vast majority of the regions within the foils in this study were found to be essentially dislocation free, indicating that no plastic

deformation had occurred in most parts of the test piece. These observations are the consequence of the fact where the applied loads were nominally elastic (Figure 3a): most regions in the bulk of the test pieces experienced stresses below the yield strength of the material and were therefore not plastically deformed. Nevertheless, there were some regions of stress raisers (such as interdendritic cast pores and nonmetallic inclusions) that were present in the bulk. Such regions were subjected to greater stresses that can be higher than the CRSS for slip, causing plastic deformation locally. The applied load led therefore to scattered plastically deformed regions within a mostly undeformed bulk.

TEM micrographs of one of these few deformed regions in the bulk are shown in Figure 4. This region was imaged using two distinct diffracting conditions and in particular using different beam directions ($[001]$ in Figure 4a and $[\bar{1}\bar{1}\bar{2}]$ in Figure 4b) and \mathbf{g} vectors ($[020]$ in Figure 4a and $[\bar{1}\bar{1}\bar{1}]$ in Figure 4b). Imaging the same region using two beam directions is an effective way to understand the 3D arrangements of dislocations, hence enabling a better understanding of plastic deformation in TEM foils. The micrographs in Figure 4 show that the matrix channels were plastically deformed during the fatigue test, while no plastic deformation occurred in the γ' precipitates. This was found to be true for all the deformed areas within the bulk

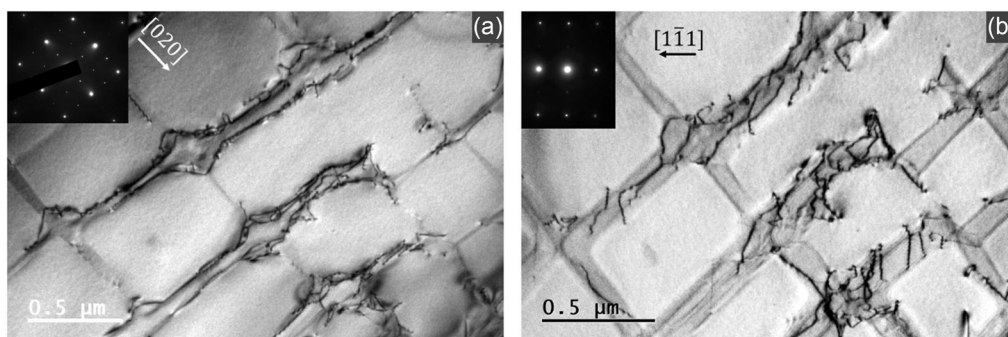


Figure 4. TEM-BF micrographs showing a plastically deformed region in the bulk of the test piece. The same region is imaged using two distinct diffracting conditions: a) was obtained with $\mathbf{B} = [001]$ and $\mathbf{g} = [020]$, whilst b) was obtained with $\mathbf{B} = [\bar{1}\bar{1}\bar{2}]$ and $\mathbf{g} = [\bar{1}\bar{1}\bar{1}]$.

including regions of local stress raisers such as cast pores. This observation of dislocation structure is in agreement with previous studies (of microstructure in fatigue) that showed some dislocations locate at the interface of γ' precipitates and matrix and react to form dislocation networks partly to accommodate the lattice mismatch.^[29,30]

3.3. Local Plasticity near the Notch

The main fatigue crack initiated from the notch (Figure 1a) due to the accumulation of local cyclic microplasticity induced by the stress concentration, eventually leading to fatigue failure. It is therefore important to carefully investigate local deformation near the notch. **Figure 5a** shows a STEM micrograph of a region lifted out from location 1. The entire foil was found to have undergone plastic deformation, in sharp contrast with what was observed in the bulk of the test piece. Most dislocations were once again found in the γ channels, but the dislocation density here was significantly higher compared to that in the bulk (Figure 4), leading to the formation of very dense dislocation tangles in the channels (Figure 5a). In addition, the γ' precipitates were found to be sheared in this region (Figure 5b), in contrast with local plasticity surrounding in stress raisers seen in the bulk (Figure 4). The dislocation density within the precipitates was, however, significantly lower than the one observed within the channels in the same region near the notch (Figure 5a). The dislocation density in the channels and in the precipitates at location 1 was estimated using the line intercept method in five TEM micrographs. The average dislocation density was found to be $1.6 \pm 0.4 \times 10^{14} \text{ m}^{-2}$ in the γ channels and $3.5 \pm 1.1 \times 10^{13} \text{ m}^{-2}$ in the γ' precipitates. It should be noted that these measurements were carried out on micrographs obtained in two-beam conditions using $\langle 111 \rangle$ reflections, as a clear observation of dislocations was not possible in multibeam conditions. Since several dislocations are expected to be invisible when using such reflections, the above measurements likely underestimated the dislocation density in both phases.

The above TEM studies were carried out postmortem and may therefore not reflect slip activity during the cyclic loading, in particular the early stages. To investigate the development of plasticity in the first few loading cycles, the deformation of the γ and γ' phases at location 1 in the first five cycles was estimated using the RVE model. Two field plots of plastic strain in the two phases after the first and the fifth cycles are shown in **Figure 6a,b**. Plastic strain was found to be confined to the γ channels after the first cycle (Figure 6a). After the fifth cycle the plastic strains in the channel were significantly more pronounced, and plastic strain gradually developed into the precipitates over the first five cycles (Figure 6b). Hence, the RVE model suggests that both phases experienced slip at this location in the fifth fatigue cycle; however, the magnitude of plastic strain in the channels was significantly larger compared to that in the precipitates. This is in agreement with the postmortem TEM results (Figure 5a), confirming that significant difference in slip activities in γ and γ' persisted throughout the fatigue life. GND densities in the two phases were calculated to quantitatively compare model predictions with results at location 1. Two field plots of the GND density after the first and the fifth cycles are shown in Figure 6c,d. The GND density was found to increase significantly in the γ channels in the first few cycles; in contrast, the model predicts that no GND density was expected to develop within the γ' precipitates throughout the first five fatigue cycles. The average GND density in the γ channels after the fifth cycle was found to be $1.6 \times 10^{12} \text{ m}^{-2}$, but the distributions were found to be quite strongly localized, with some regions of the γ channel having no GND evolution, reflecting plastic inhomogeneity and anisotropy. Peak values of GND density in the channels were found to be $\approx 1.0 \times 10^{13} \text{ m}^{-2}$, closer therefore to the experimental measurements (which were for the total dislocation density). Also, it is noted that the experimental measurements were carried out after many more fatigue cycles than for the RVE models, suggesting that most of dislocations generated in the first cycles and the dislocation density remained mostly unchanged. The model also enables the calculation of slip accumulation on each of the 12 octahedral slip systems in both phases at the end of the fifth

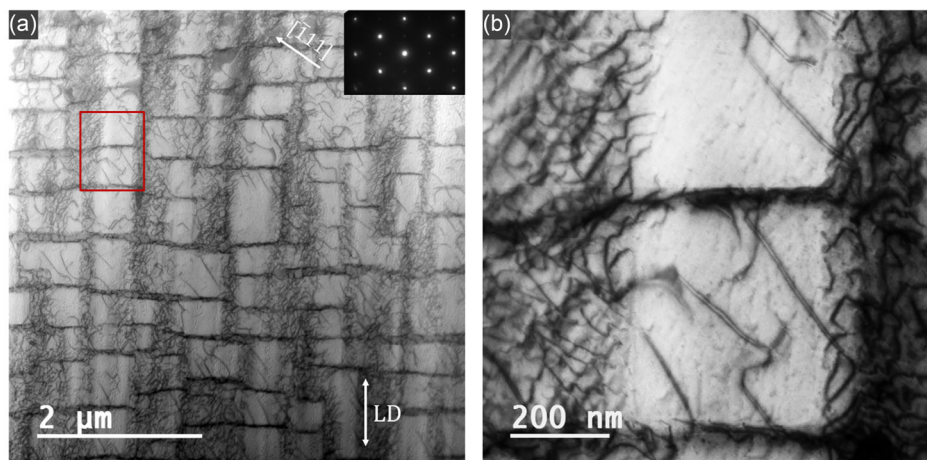


Figure 5. STEM-BF micrographs showing dislocation arrangements in a rather large region near the a) notch and b) magnified view of the region indicated by the red rectangle. These images were formed with $\mathbf{B} = [110]$ and $\mathbf{g} = [\bar{1}11]$. The LD is indicated in (a). This TEM foil was lifted out in location 1. Adapted with permission from our previous work,^[32] Copyright 2020, Springer Nature.

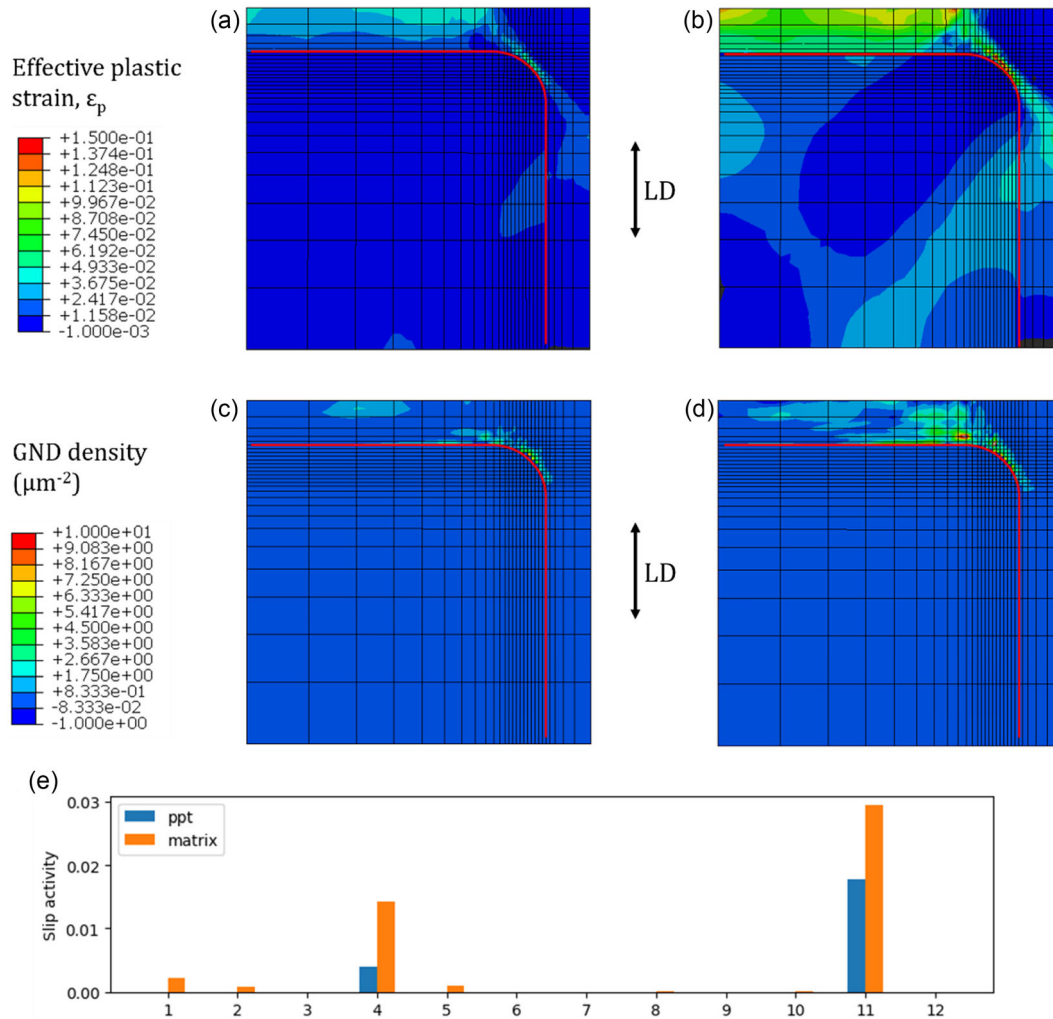


Figure 6. Plastic strain field plots through a midsection of the RVE at location 1 after the a) first cycle and b) after the fifth cycle. GND density (μm^{-2}) field plots are shown after c) the first cycle and d) the fifth cycle. The red line denotes the interface between γ and γ' , while LD indicates the loading direction. e) The average slip on each slip system through γ and γ' precipitates (denoted by “ppt”) after five cycles.

fatigue cycle, as shown in Figure 6e. Slip is predicted to occur to a greater extent in the channels compared to the precipitates: five slip systems were active in the γ channels, and in particular slip systems 1, 2, 4, 5, and 11. The two most active slip systems in the γ channels (slip systems 4 and 11) were seen to be active in the γ' precipitate. The fraction of the total shear strain on each slip system within each phase was calculated to estimate the relative amount of slip between the two phases: 72% of slip was found to occur in the matrix channels, with only 28% occurring in the precipitate phase.

Most interestingly, the dislocations within γ' had distinctive arrangement, as shown in Figure 5a. Such aligned dislocations are found to be dislocation pairs rather than individual dislocations, as shown in the magnified STEM micrograph in Figure 5b. In addition, a second set of aligned dislocation pairs was found within the γ' precipitates. The two sets can be observed separately in Figure 7, which includes two micrographs of the same precipitate obtained using two different two-beam conditions. It should

be noted that the micrographs in Figure 7 are rotated with respect to those in Figure 5. The diffraction patterns and LDs are indicated in both Figure 5 and 7 for comparisons. Figure 7a was obtained using the same conditions as the micrographs in Figure 5; therefore, the set lying on the $(\bar{1}\bar{1}1)$ trace was visible, while the second one was invisible (as in Figure 5). However, when the $[\bar{1}\bar{1}\bar{1}]$ diffraction vector was used, the first set of dislocation pairs became invisible and a second set became visible (Figure 7b). The pairs in this second set were once again aligned with one another and appeared to lie on the trace of the $(\bar{1}\bar{1}1)$ plane.

To summarize, the dislocation arrangements observed in location 1 consisted of very dense dislocation tangles in the matrix channels and two sets of aligned dislocation pairs within the γ' precipitates. The same dislocation arrangements were observed in two additional foils lifted out from locations 2 and 3. In other words, these dislocation arrangements were consistently seen in all the foils lifted out from the fatigue crack initiation region

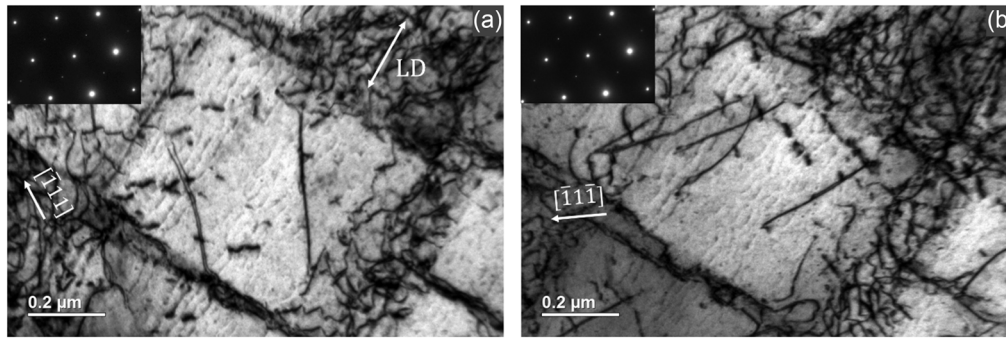


Figure 7. TEM-BF micrographs showing the same precipitate imaged using two distinct diffracting conditions, which only allow a single set of dislocation pairs to be visible in each image. Both images were obtained with $\mathbf{B} = [110]$; however, $\mathbf{g} = [\bar{1}11]$ was used in a) and $\mathbf{g} = [\bar{1}\bar{1}\bar{1}]$ was used in b). The LD is indicated in (a). This TEM foil was lifted out at location 1.

surrounding the notch. This observation is particularly interesting at location 3, the farthest from the notch (Figure 1), where the effect of the notch may have been less pronounced, and plasticity may have been related more directly with the early stage of crack propagation.

The above observations were repeatable at several locations near the notch. However, the foils for locations 1–3 were lifted out directly from the fracture surface; thus, the LD was contained in the plane of the foils. One further FIB lift-out was needed to obtain a foil that was normal to the LD and therefore confirms the dislocation arrangements. A foil was lifted out at location 4 shown in Figure 1c. TEM-BF micrographs of two regions within this foil are shown in Figure 8. These micrographs show once again the familiar dislocation pairs within γ' , together with the higher dislocation density in the matrix channels. Furthermore, the dislocation pairs were consistently aligned with one another; these observations are in good agreement with those previously made with foils parallel to the LD (e.g., Figure 5), with the exception that a single dominant set of aligned dislocation pairs was seen in this last foil.

All the above micrographs support the conclusion that dislocation activity within γ' precipitates, in the form of aligned dislocation pairs, was rather extensive in regions close to the notch. Such observations are in contrast with those made in the bulk of the test pieces, where dislocations were entirely confined to the matrix channels (Figure 4). Since they populate the

initiation region, these dislocations pairs may have played a major role in fatigue crack initiation in this test piece and deserved a thorough examination, in particular to determine the Burgers vector and line direction and hence the character, of the dislocations lying within γ' . Such an examination (shown in Appendix B) revealed that the dislocation pairs observed in the foil extracted at location 1 on the trace of the $(\bar{1}11)$ plane were characterized by $\mathbf{b} = \pm[0\bar{1}1]$ and $\mathbf{u} = [0\bar{1}1]$; since \mathbf{b} was parallel to \mathbf{u} , the dislocations forming the pairs were screw in character. Both octahedral and cube slip can occur at high temperatures in Ni-based superalloys.^[45,46] One further characterization effort was therefore necessary to determine whether these pairs were lying on the octahedral $(\bar{1}11)$ or on the cube (100) plane. Two useful micrographs in this regard are shown in Figure 9. Here, the same region is imaged using two distinct beam directions to enable a 3D interpretation of the dislocation arrangements. This is somewhat similar to the technique used for the two micrographs in Figure 4; however, the same \mathbf{g} reflection was used here to form the two images. This removes ambiguity associated with diffraction contrast, as any difference in the two micrographs can only be attributed to the tilt angle between the two zone axes. The micrographs in Figure 9 show that the second dislocation in the pair “disappears” behind the first one on the trace of the $(\bar{1}11)$ plane when $\mathbf{B} = [110]$, while both dislocations can be easily resolved when $\mathbf{B} = [2\bar{1}1]$ (in this case the $(\bar{1}11)$ plane is not normal to the plane of the micrograph). This shows

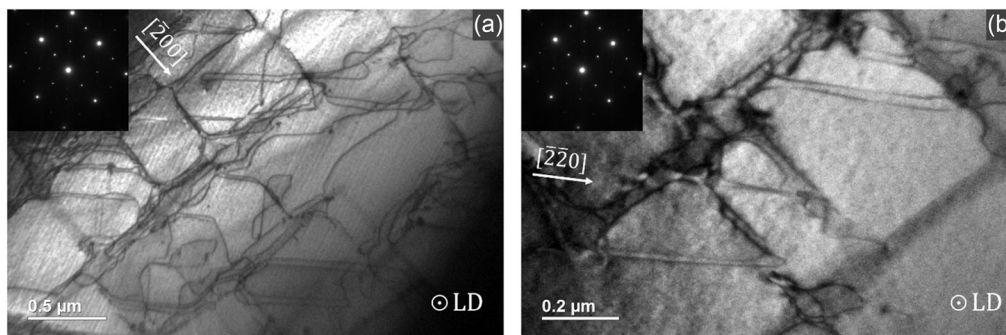


Figure 8. TEM-BF micrograph showing two regions within the foil lifted out from location 4. Both images were obtained with $\mathbf{B} = [00\bar{1}]$; however, $\mathbf{g} = [\bar{2}00]$ was used in a) and $\mathbf{g} = [\bar{2}\bar{2}0]$ was used in b). The LD is indicated in the micrographs.

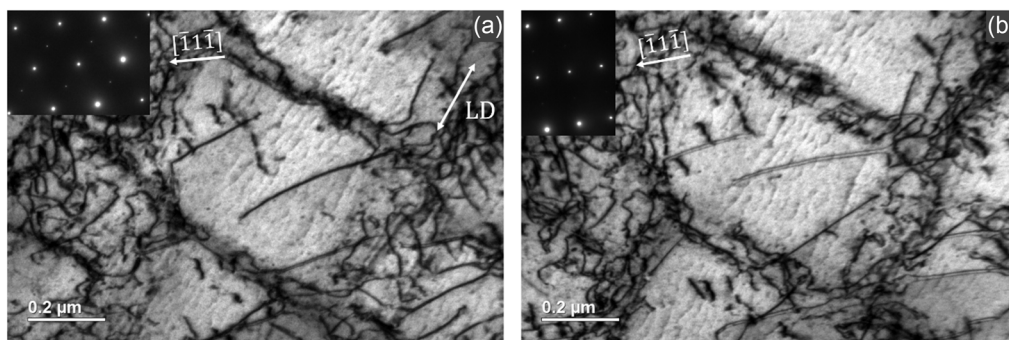


Figure 9. TEM-BF micrographs showing the same region imaged using two distinct diffracting conditions. Both images were obtained with $\mathbf{g} = [\bar{1}\bar{1}\bar{1}]$. However, $\mathbf{B} = [110]$ was used in a) and $\mathbf{B} = [2\bar{1}\bar{1}]$ was used in b). The LD is indicated in (a). This TEM foil was lifted out at location 1.

that the dislocation pairs were lying on the $(\bar{1}11)$ plane and belonged therefore to the octahedral slip system 11, that is, $(\bar{1}11)[0\bar{1}1]$. The same analyses were carried out on the second set of aligned dislocation pairs seen at location 1 (not shown here); it showed that $\mathbf{b} = \pm[011]$ and $\mathbf{u} = [011]$, and therefore that the second active slip system in γ' was $(\bar{1}\bar{1}1)[011]$ (slip system 5). The above observations show that only two slip systems were active in γ' at location 1 during cyclic loading. Although such complete analyses were not conducted in regions 2 and 3, it could be argued that the same two slip systems were active in these regions, since the dislocation pairs were lying along the same directions and became invisible with the same reflections, as shown in our previous work.^[32] On the other hand, the dislocations in the single set observed in the foil extracted on the fracture surface cross section (location 4, Figure 8) were found to have $\mathbf{b} = \pm[101]$ and $\mathbf{u} = [110]$. Hence, these dislocations were mixed in character and belonged to the octahedral slip system 10, that is, $(\bar{1}11)[101]$. Thus, only octahedral slip was observed within γ' precipitates in all regions near the notch.

The γ/γ' RVE model allowed the calculation of the slip activities in the γ' phase at the four locations of interest during the first few loading cycles. Table 5 presents the results of such calculation at the end of the fifth loading cycle. The model predictions showed some agreement with experimental TEM observation of slip activities. TEM results and model predictions were in good agreement at location 1: the model predicted slip system 11 to be the most active at this location (Table 5), and the same slip system was observed experimentally (Figure 5b). However, the CPFEM interestingly suggested that slip systems were activated in the γ' phase depending on the location relative to the notch, showing

Table 5. Predictions of effective plastic strain on active slips system in the γ' phase at the locations of interest after five fatigue cycles obtained using the RVE model. The unlisted slip systems did not exhibit slip activity in the γ' phase at the considered locations. Location 3 is not listed as the model predicted no slip activity within the γ' phase at the end of the fifth loading cycle.

Slip system	1	4	5	11
Location 1	–	0.004	–	0.018
Location 2	0.012	–	–	–
Location 4	–	0.024	0.024	0.132

differences between the CPFEM prediction and TEM observation. In particular, the activation of system 5 observed by TEM was not predicted by the model at location 1; instead, the model suggests the activation of slip system 4. Slip systems 5 and 11 were observed by TEM at location 2; however, the model only predicted the activation of slip system 1. Finally, there was no agreement at location 4, since the TEM results showed the activation of slip system 10 only. Such differences between TEM results and modeling predictions mostly related to the fact that while the model only considered the first five loading cycles, TEM investigations were carried out postmortem and therefore after a significantly higher number of loading cycles. During these cycles, the high stresses near the notch induced local dislocation multiplication as well as to-and-fro motion of such dislocations; the interactions between mobile dislocations led to significant hardening of some active slip systems and thus alter the slip activity evolution. This effect led to a considerable modification of slip activity during the fatigue life of the specimen, explaining the disagreements above. In addition, it is worth mentioning that slip system identification via TEM is inevitably affected by the unloading of samples and only dislocations that were arrested in the γ' phase were observed by TEM while others that completely sheared through the γ' phase would not be seen in TEM investigations.

4. Discussions

Dislocation activity was confined to the γ channels in the few deformed regions near stress raisers (such as low-angle grain boundaries and inclusions) in the bulk of the fatigued test piece (Figure 4); this suggests that such stress concentrations in the bulk only had moderate effects and were not sufficient to shear the γ' precipitates, which are significantly stronger than the γ matrix channels at 800 °C.^[47] In contrast the CPFEM showed that the introduced notch caused substantial increase in loads, even 2 and 3 times larger than the nominal one, resulting in significant plastic strains starting right from the very first fatigue cycle (Figure 3b) and thereby in extensive deformation of both phases, as consistently shown by STEM investigations (Figure 5) and model results (Figure 6). CPFEM allows additional insights into dislocation slip activities (hence local plasticity) in the first few cycles. In detail, dislocation slip occurred only in the γ channels

(Figure 6a), and then progressed into the precipitates after a few cycles (Figure 6b). This indicates that even the high local stresses were initially not sufficient to shear the strong γ' precipitates right away; instead, γ' shearing occurred subsequently as a considerable pile up of dislocations in the channels, which locally raised the stresses enough to induce a slip transmission into the precipitates.^[48,49] It has been known that the deposition and subsequent reactions of dislocations at the γ/γ' interface in the plasticity-assisted creep of nickel superalloys at high temperatures create superdislocations that shear γ' driven by the increase in stress field induced by the following dislocations of the same slip system.^[49–51] Extended faults (that are typically observed when superdislocations shear γ' ^[52,53]) were not seen in our observations due to the orientation of observations similar to what was shown in another study.^[51] It is likely that the same dislocation reaction as seen in ref. [50] was also applicable in this current study. These observations are supported by the fact that the model predicted slip in the precipitates only on the most active slip systems in the matrix (Figure 6e) and by postmortem TEM observations, which showed significantly higher dislocation densities in the channels compared to the precipitates (e.g., Figure 5b). It is worth noting that the degree of plasticity at a specific location is only one factor governing the location of crack initiation or the direction of crack propagation.^[54] Therefore, a high level of plasticity does not necessarily indicate the propagation direction of crack.

The deformation of the γ' phase generally occurs via $a\langle 110 \rangle$ superdislocations, which are known to dissociate following a number of mechanisms.^[55] Careful TEM studies showed that γ' shearing occurred via dislocation pairs near the notch (e.g.,

Figure 5b); in addition, both partials in each pair were characterized by the same $\langle 110 \rangle$ Burgers vectors (see Appendix B). The pairs were therefore composed of $a/2\langle 110 \rangle$ dislocations separated by antiphase boundaries (APBs), that is, the regions where the chemical ordering of the γ' phase is disrupted by the leading partials.^[56] The APB dissociation is the most commonly observed in superalloys and a key contributor to their outstanding strength, particularly at high temperatures,^[55,57] explaining the large stresses needed to activate slip in the γ' precipitates.

Most common explanation for the development of plasticity in γ' surrounding a stress raiser (including a notch) has been linked to the increased stresses near the notch. An additional fatigue test without a notch was carried out with the same conditions except with a higher strain amplitude (1.2%) to investigate whether increasing the applied stress alone would induce the same microstructural deformation modes observed in the initiation region of the notched sample. The strain amplitude of 1.2% was selected as it was close to the largest one experienced by the location 4 near the notch (Figure 3b). TEM micrographs of this additional test piece are shown in Figure 10. There was a significantly higher number of dislocations in both γ and γ' of this sample (Figure 10a), confirming that the high dislocation density was due to the increase in the applied stress. However, the arrangement of dislocations in γ' was distinctively different to that in the surrounding of the notch of the loading, in particular in the location 4 of the sample tested at the lower strain amplitude of 0.6% (Figure 10 versus 7–9). There were some unpaired dislocations observed in γ' (Figure 10b). While dislocation arrangement appeared to be complex in some high-density regions of

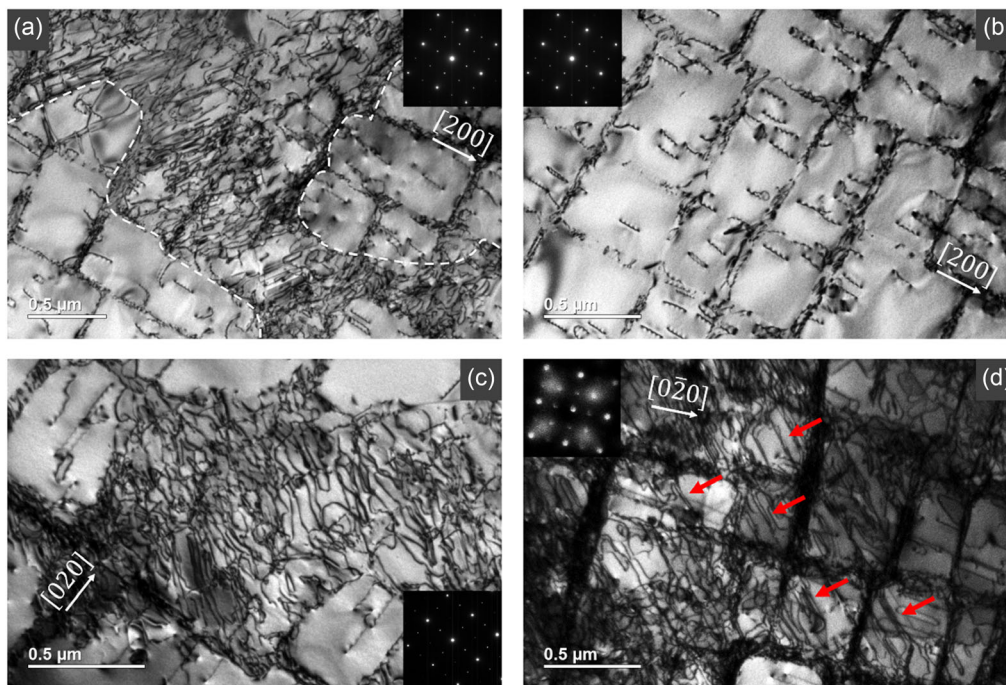


Figure 10. TEM-BF micrographs from a fatigue specimen tested at 800 °C with a 1.2% strain amplitude. Images a,b) were obtained with $\mathbf{B} = [00\bar{1}]$ and $\mathbf{g} = [200]$, image c) with $\mathbf{B} = [00\bar{1}]$ and $\mathbf{g} = [020]$, and image d) with $\mathbf{B} = [00\bar{1}]$ and $\mathbf{g} = [0\bar{2}0]$. The white dashed lines in (a) separate regions with either high or low dislocation density within γ' precipitates. The red arrows in (d) indicate dislocation pairs within γ' precipitates. The LD was out of plane in all micrographs.

dislocations in γ' (Figure 10c), it was not the same to those observed in regions surrounding the notch of the lower strain amplitude (e.g., Figure 5a). This difference suggests that the locally increased stresses alone could explain the high dislocation densities and γ' shearing, but not the distinctive dislocation arrangements. This therefore shows the key role played by the local variation in both multiaxial stress state in addition to the increased stresses. Moreover, different locations surrounding the notch experienced different degrees of strain over the same time duration of loading (Figure 3b), that is, they experienced different loading rates. Variations in the loading rate change the kinetics of dislocation slip; and hence, the dislocation interactions and subsequently dislocation arrangements. In addition, the loading rates also affect the chemical segregation that is found to be a governing factor in the shearing of precipitates in nickel superalloys.^[58] Therefore, different loading rates near the notch might also play some influential roles in the dislocation arrangements. Consequently, the combination of both the multiaxial stress states and loading rates is believed to be also responsible for the distinctive dislocation arrangements in the notch vicinity (e.g., Figure 5a).

In addition, despite the shearing mechanism being the same at all locations near the notch, the identification of distinct slip activations within γ' precipitates by TEM studies highlighted the effect of the spatial variation of the locally modified stress state induced by the notch, in agreement with CPFEM model predictions (Section 3.1 and Table 5) and with reports in the literature.^[8,9] Hence, the results of this work show that local plasticity near the notch was a complex function of the increased stresses, increased loading rates, multiaxial stress states, and their spatial variation around the notch and that it differed significantly from both bulk plasticity in the notched sample and from bulk plasticity in a sample tested with larger cyclic loads. Because the regions near the notch experienced larger strains compared to the bulk over the same duration of time (Figure 3), the strain rate of the regions must be higher. In fact, the simulation showed that location 4 experienced the largest strain rate of $1.2 \times 10^{-2} \text{ s}^{-1}$, more than double the nominal strain rate of $5.0 \times 10^{-3} \text{ s}^{-1}$. It is similar to other locations surrounding the notch. It is likely that the increase in loading rates and the reversibility of dislocation slip in regions surrounding the notch are responsible for the distinctive arrangement of dislocations observed in the γ' precipitates.

5. Conclusion

This study presents the first TEM-based site-specific investigation of local cyclic plasticity developing in the crack initiation region in a notched Ni-based single-crystal superalloy subjected to fatigue testing at 800 °C. Postmortem experimental studies were coupled with microstructure-based CPFEM modeling to obtain insights into the development of dislocation slip and local plasticity in the first few cycles: 1) There are distinctive differences in local slip activities in regions surrounding the notch in comparison to the bulk. Although the nominal loading was elastic, there were some isolated bulk plasticity confined to the γ channels due to local stress raisers such as inclusions and low-angle grain boundaries. In contrast, local plasticity near

the notch featured high dislocation densities in the γ channels, dislocations shearing the γ' precipitates, and, most interestingly, distinctive arrangements of dislocation pairs in γ' ; 2) Slip in γ' near the notch was shown to occur on octahedral systems by means of dislocation pairs separated by antiphase boundaries. Few slip systems were found to be active at each of the locations investigated, and the active slip systems varied at different locations, highlighting the spatial variation of the stress field around the notch as confirmed by CPFEM simulation results. The RVE model also showed that the local stress fields near the notch led to considerable microplasticity starting from the very first loading cycle, initially developing in the γ channels, and dislocations on most active slip system subsequently progressed to shear into the γ' precipitates; and 3) Finally, bulk plasticity investigations with larger nominal cyclic strains showed that the locally increased stresses near the notch could explain the high dislocation densities and the shearing of γ' but not the distinctive dislocation arrangements near the notch. It is suggested that the variation in loading rates and the reversibility of dislocation slip in different regions surrounding the notch are largely responsible for the distinctive arrangement of dislocations observed in the γ' precipitates in the nominally elastic cyclic loading.

The results of this work provide new fundamental insights into the development of local plasticity near stress concentrations and emphasize the need for further local deformation studies toward an improved understanding of fatigue crack initiation in Ni-based single-crystal superalloys.

Appendix

Appendix A. Tensile data: experiment and model

To validate the parameters selected for the RVE model, stress/strain data from a tensile test were generated and compared with experimental data. A comparison between the two sets of data is shown in Figure A.1, which shows reasonably good agreement between the experimental results and the model predictions.

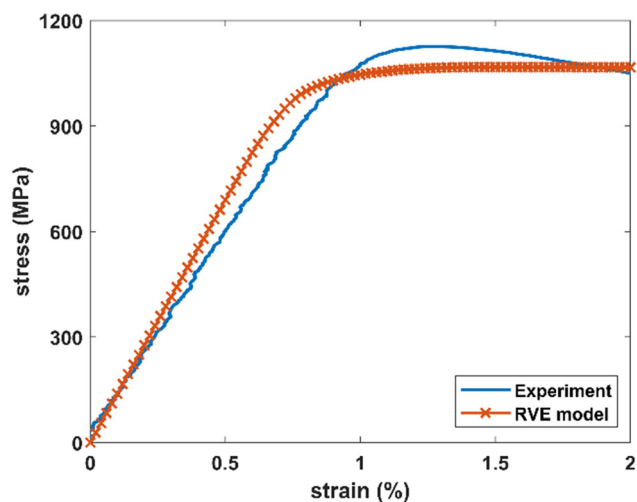


Figure A.1. Comparison between the experimental stress/strain curve from a tensile test carried out at 800 °C with a strain rate of 10^{-3} s^{-1} and that generated with the RVE model.

Acknowledgements

The authors gratefully acknowledge the support received from the Beijing Institute of Aeronautical Materials (BIAM). The research was performed at the BIAM-Imperial Centre for Materials Characterisation, Processing and Modelling at Imperial College London.

Conflict of Interest

The authors declare no conflict of interest.

Data Availability Statement

The data that support the findings of this study are available from the corresponding author upon reasonable request.

Keywords

crystal plasticity modeling, dislocations, electron microscopy, fatigue, nickel alloys

Received: April 26, 2023

Revised: October 21, 2023

Published online: November 27, 2023

- [1] T. J. Carter, *Eng. Failure Anal.* **2005**, *12*, 237.
- [2] P. K. Wright, M. Jain, D. Cameron, *Superalloys* **2004**, *2004*, 657.
- [3] L. Rémy, M. Geuffrard, A. Alam, A. Köster, E. Fleury, *Int. J. Fatigue* **2013**, *57*, 37.
- [4] Y. Takahashi, D. Kobayashi, M. Kashihara, T. Kozawa, S. Arai, *Mater. Sci. Eng. A* **2020**, *793*, 139821.
- [5] D. W. MacLachlan, D. M. Knowles, *Fatigue Fract. Eng. Mater. Struct.* **2001**, *24*, 503.
- [6] B. Rutttert, C. Meid, L. Mujica Roncery, I. Lopez-Galilea, M. Bartsch, W. Theisen, *Scr. Mater.* **2018**, *155*, 139.
- [7] H. Z. Mao, Z. X. Wen, Z. F. Yue, B. Z. Wang, *Mater. Sci. Eng. A* **2013**, *587*, 79.
- [8] N. K. Arakere, S. Siddiqui, F. Ebrahimi, *Int. J. Solids Struct.* **2009**, *46*, 3027.
- [9] P. A. Sabnis, M. Mazière, S. Forest, N. K. Arakere, F. Ebrahimi, *Int. J. Plast.* **2012**, *28*, 102.
- [10] H. Zhou, X. Zhang, P. Wang, S. Lu, *Int. J. Plast.* **2019**, *119*, 249.
- [11] E. Fleury, L. Rémy, *Mater. Sci. Eng. A* **1993**, *167*, 23.
- [12] M. Ramsperger, R. F. Singer, C. Körner, *Metall. Mater. Trans. A* **2016**, *47*, 1469.
- [13] B. Attard, S. Cruchley, C. Beetz, M. Megahed, Y. L. Chiu, M. M. Attallah, *Addit. Manuf.* **2020**, *36*, 101432.
- [14] P. Fernandez-Zelaia, M. M. Kirka, A. M. Rossy, Y. Lee, S. N. Dryepondt, *Acta Mater.* **2021**, *216*, 117133.
- [15] A. Piglione, B. Attard, V. Vieira Rielli, C.-T. Santos Maldonado, M. M. Attallah, S. Primig, M.-S. Pham, *Addit. Manuf.* **2021**, *47*, 102347.
- [16] M. Jin, A. Piglione, B. Dovggy, E. Hosseini, P. A. Hooper, S. R. Holdsworth, M.-S. Pham, *Addit. Manuf.* **2020**, *36*, 101584.
- [17] N. Sanaei, A. Fatemi, *Theor. Appl. Fract. Mech.* **2020**, *108*, 102638.
- [18] L. Zhang, L. G. Zhao, A. Roy, V. V. Silberschmidt, G. McColvin, *Mater. Sci. Eng. A* **2019**, *744*, 538.
- [19] X. G. Wang, J. L. Liu, T. Jin, X. F. Sun, Y. Z. Zhou, Z. Q. Hu, J. H. Do, B. G. Choi, I. S. Kim, C. Y. Jo, *Scr. Mater.* **2015**, *99*, 57.
- [20] W. W. Milligan, N. Jayaraman, R. C. Bill, *Mater. Sci. Eng.* **1986**, *82*, 127.
- [21] L. Liu, J. Meng, J. Liu, H. Zhang, X. Sun, Y. Zhou, *Mater. Sci. Eng. A* **2018**, *734*, 1.
- [22] L. Liu, J. Meng, J. Liu, T. Jin, X. Sun, H. Zhang, *Mater. Des.* **2017**, *131*, 441.
- [23] P. Li, Q. Q. Li, T. Jin, Y. Z. Zhou, J. G. Li, X. F. Sun, Z. F. Zhang, *Int. J. Fatigue* **2014**, *63*, 137.
- [24] U. Glatzel, M. Feller-Kniepmeier, *Scr. Metall. Mater.* **1991**, *25*, 1845.
- [25] V. Brien, B. Décamps, *Mater. Sci. Eng. A* **2001**, *316*, 18.
- [26] G. E. Dieter, *Mechanical Metallurgy*, McGraw Hill, New York, USA **1988**.
- [27] D. F. Lahrman, R. D. Field, R. Darolia, H. L. Fraser, *Acta Metall.* **1988**, *36*, 1309.
- [28] R. Field, T. Pollock, W. Murphy, *Superalloys* (Eds: R. W. S. S. D. Antolovich, R. A. MacKay, D. L. Anton, T. Khan, R. D. Kissinger, D. L. Klarstrom), TMS **1992**, p. 557.
- [29] J. H. Zhang, Z. Q. Hu, Y. B. Xu, Z. G. Wang, *Metall. Trans. A* **1992**, *23*, 1253.
- [30] T. P. Gabb, R. V. Miner, J. Gayda, *Scr. Metall.* **1986**, *20*, 513.
- [31] A. Cervellon, S. Hémerly, P. Kürsteiner, B. Gault, P. Kontis, J. Cormier, *Acta Mater.* **2020**, *188*, 131.
- [32] A. Piglione, J. Yu, J. Zhao, C. Xiao, F. Dunne, M.-S. Pham, *Superalloys* **2020**, *2020*, 333.
- [33] J. R. Li, Z. G. Zhong, S. Z. Liu, D. Z. Tang, P. Wei, P. Y. Wei, Z. T. Wu, D. Huang, M. Han, *Superalloys* **2000**, *2000*, 777.
- [34] M. S. Pham, C. Solenthaler, K. G. F. Janssens, S. R. Holdsworth, *Mater. Sci. Eng. A* **2011**, *528*, 3261.
- [35] R. K. Ham, *Philos. Mag.* **1961**, *6*, 1183.
- [36] J. W. Edington, *Practical Electron Microscopy in Materials Science*, Macmillan, London **1976**.
- [37] F. P. E. Dunne, D. Rugg, A. Walker, *Int. J. Plast.* **2007**, *23*, 1061.
- [38] J. Cheng, S. Ghosh, *Int. J. Plast.* **2015**, *67*, 148.
- [39] E. Balicki, A. Raman, R. A. Mirshams, *J. Mater. Eng. Perform.* **2000**, *9*, 324.
- [40] B. Chen, J. Jiang, F. P. E. Dunne, *Int. J. Plast.* **2018**, *101*, 213.
- [41] D. Siebörger, H. Knake, U. Glatzel, *Mater. Sci. Eng. A* **2001**, *298*, 26.
- [42] F. E. Heredia, D. P. Pope, *Acta Metall.* **1986**, *34*, 279.
- [43] A. Nitz, E. Nembach, *Metall. Mater. Trans. A* **1998**, *29*, 799.
- [44] N. Clément, A. Coujou, M. Jouiad, P. Caron, H. Kirchner, T. Khan, *Superalloys* **1996**, *1996*, 239.
- [45] A. E. Staton-Bevan, R. D. Rawlings, *Phys. Status Solidi A* **1975**, *29*, 613.
- [46] A. W. Mello, A. Nicolas, M. D. Sangid, *Mater. Sci. Eng. A* **2017**, *695*, 332.
- [47] D. P. Pope, S. S. Ezz, *Int. Met. Rev.* **1984**, *29*, 136.
- [48] W. W. Milligan, S. D. Antolovich, *Metall. Trans. A* **1987**, *18A*, 85.
- [49] Y. M. Eggeler, K. V. Vamsi, T. M. Pollock, *Ann. Rev. Mater. Res.* **2021**, *51*, 209.
- [50] L. Agudo Jácome, P. Nörtershäuser, C. Somsen, A. Dlouhý, G. Eggeler, *Acta Mater.* **2014**, *69*, 246.
- [51] R. Srinivasan, G. F. Eggeler, M. J. Mills, *Acta Mater.* **2000**, *48*, 4867.
- [52] V. Sass, U. Glatzel, M. Feller-Kniepmeier, *Acta Mater.* **1996**, *44*, 1967.
- [53] M. Li, M.-S. Pham, Z. Peng, G. Tian, B. A. Shollock, *Mater. Sci. Eng. A* **2018**, *718*, 147.
- [54] V. V. C. Wan, D. W. MacLachlan, F. P. E. Dunne, *Int. J. Fatigue* **2014**, *68*, 90.
- [55] W. W. Milligan, S. D. Antolovich, *Metall. Trans. A* **1991**, *22A*, 2309.
- [56] R. C. Reed, *The Superalloys: Fundamentals and Applications*, Cambridge University Press, Cambridge **2006**.
- [57] D. Barba, A. J. Egan, Y. Gong, M. J. Mills, R. C. Reed, in *Superalloys* (Eds: S. Tin, M. Hardy, J. Clews, J. Cormier, Q. Feng, J. Marcin, C. O'Brien, A. Suzuki), Springer International Publishing, Cham **2020**, p. 260.
- [58] D. Barba, T. M. Smith, J. Miao, M. J. Mills, R. C. Reed, *Metall. Mater. Trans. A* **2018**, *49*, 4173.